

X-ray emission measurements following charge exchange between C^{6+} and H_2

M. Fogle*

Department of Physics, Auburn University, Auburn, Alabama 36849

D. Wulf, K. Morgan, and D. McCammon

Department of Physics, University of Wisconsin, Madison, Wisconsin 53706

D. G. Seely

Department of Physics, Albion College, Albion, Michigan

I. N. Draganić and C. C. Havener

Physics Division, Oak Ridge National Laboratory, Oak Ridge, Tennessee 37831

(Dated: December 3, 2024)

Lyman x-ray spectra following charge exchange between C^{6+} and H_2 are presented for collision velocities between 400 and 2300 km/s (1–30 keV/amu). Spectra were measured by a microcalorimeter x-ray detector capable of fully resolving the C VI Lyman series emission lines through Lyman- δ . The ratios of the measured emission lines are sensitive to the angular momentum l -states populated during charge exchange and are used to gauge the effectiveness of different l -distribution models in predicting Lyman emission due to charge exchange. At low velocities, we observe that both single electron capture and double capture autoionization contribute to Lyman emission and that a statistical l -distribution best describes the measured line ratios. At higher velocities single electron capture dominates with the l -distribution peaked at the maximum l .

PACS numbers: 34.70.+e, 32.30.-r, 95.30.-k

I. INTRODUCTION

Charge exchange (CX) between highly charged ions and atomic and molecular targets can exhibit large cross sections (10^{-15} cm²) at certain collision velocity regimes, making it one of the dominant processes in plasma environments. The resulting emission lines due to cascading captured electrons can provide temperature, density and relative abundance information about the interaction environment. In laboratory magnetic confinement plasmas, CX is a common diagnostic tool used in combination with puffed gas and neutral beams injection [1–3]. In astrophysical settings, the identification of x-ray emission from comets has been linked to CX between solar wind ions and ablated cometary neutral gases [4–6]. These same solar wind ions interact with neutrals of planetary atmospheres and from the heliosphere. These applications have made CX modeling of paramount interest to both the laboratory plasma and astrophysics communities.

A successful model of emission spectra due to CX relies on being able to map the specific distribution of principal, n , and angular momentum, l , quantum states in which the transferred electron is captured on the ion. Several successful tools have been developed to estimate the n -state of capture, however, the state-selective n, l CX cross sections are highly dependent on collision velocity and several models, of various effectiveness, have been put forth to estimate the l -distributions in CX over different collision velocity regimes.

A number of previous theoretical and experimental studies helped to establish methods of determining CX cross sections and the principle quantum state n of capture for given interaction pairs and energies. In the regime where the collision velocity is approximately equal to the orbital velocity of the captured electron, the most successful tool has been the classical over-the-barrier model (CBM) [7]. At higher collision velocities, the classical trajectory Monte Carlo (CTMC) technique has shown to be successful [8]. At lower collision velocities, the CX process involves complex trajectories and interaction dynamics between many states and is best modeled by atomic orbital (or molecular orbital) close-coupling (AOCC, MOCC) methods [9, 10]. Given that these calculations involve multiple electrons (and nuclei) they are inherently difficult and have not been widely adapted for extended use in CX modeling. It should also be noted that at these slower collision velocities, transfer ionization (TI), stabilized double capture (DC) and double

*fogle@physics.auburn.edu

capture autoionization (DCAI) can contribute to the total CX cross section in addition to the normal single electron capture (SEC) mechanism. These additional processes are rarely included in CX models.

The most prolific l -distribution models from the literature [11, 12] have been *i*) an even distribution, in which the l -states are evenly distributed across an n -manifold based on the total number of angular momentum states available, *ii*) a statistical distribution given by

$$\frac{2l+1}{n^2}, \quad (1)$$

iii) a Landau-Zener (LZ) distribution given by

$$\frac{l(l+1)(2l+1)(n-1)(n-2)!}{(n+l)!(n-l-1)!} \quad (2)$$

and *iv*) a separable distribution given by

$$\frac{2l+1}{Z} \exp\left(\frac{-l(l+1)}{Z}\right) \quad (3)$$

where Z is the charge of the capturing ion. In general, a statistical distribution is usually assumed to become dominant when the collision velocity is approximately half the orbital velocity of the captured electron [13]. At slower collision velocities the l -distribution tends to be either even or peaked at intermediate l -states, such as in the separable and LZ distributions above. At higher collision velocities, the l -distribution migrates to preferentially higher l -states in what is typically termed an *over-statistical* distribution with a majority of captured electrons in the maximum l -state. None of the l -distribution models above describe this over-statistical distribution.

Here we report the measurement of Lyman emission lines resulting from the CX interaction between C^{6+} and H_2 using a high resolution microcalorimeter x-ray detector. From these measured emission lines, we investigate the effect of collision velocity on the state-selective l -distributions during the capture process by determining line ratios between Lyman-alpha (L_α), Lyman-beta (L_β) and Lyman-gamma (L_γ) emission lines.

Total CX cross sections for C^{6+} on H_2 and He have been measured by Meyer et al. [14, 15] and Greenwood et al. [16]. Few state-resolved CX experiments, however, have been conducted for C^{6+} on H_2 . Dijkkamp et al. [17] utilized vacuum ultraviolet (VUV) spectroscopy to investigate the state-resolved l -distributions of CX for C^{6+} , N^{6+} and O^{6+} on He and H_2 , however, their results for C^{6+} on H_2 were inconclusive due to high relative uncertainties and unavoidable state degeneracies related to the observed emission lines. Hoekstra et al. [18] repeated the VUV measurements of Dijkkamp et al. with a refined experimental apparatus with specific aim to investigate the relative n capture states via SEC and DCAI. Mack et al. [19, 20] measured correlation effects of double capture between C^{6+} and H_2 . Recently, we reported high resolution Lyman emission measurements resulting from CX between C^{6+} and He using the microcalorimeter apparatus discussed here [21]. All of these previous results clearly show that even though H_2 and He are both strict two-electron systems, the ionization potential of the target is the primary parameter that governs the n -state capture. For the He target, the principal capture in C^{6+} is to $n=3$, which is confirmed by the CBM. For H_2 , the principal capture state is $n=4$, also confirmed by the CBM. The l -distributions, however, are not so easily estimated at different collision velocity regimes. It is the intent here to provide further information on the velocity dependence of CX between C^{6+} and H_2 with regard to the capture l -states.

II. EXPERIMENT

The charge exchange emission spectra of C^{6+} on H_2 were measured by adapting the ion-atom merged beams apparatus at Oak Ridge National Laboratory [22] with an X-ray microcalorimeter detector from the University of Wisconsin and Goddard Space Flight Center sounding rocket experiment to measure Lyman emission from the resulting H-like C^{5+} ion. A schematic of the experimental apparatus can be seen in Fig. 1 and has been discussed previously [21]. The ion beam of $^{13}C^{6+}$ was produced by an electron cyclotron resonance (ECR) ion source with ^{13}CO as the working gas. Isotopic carbon was selected to avoid ion beam contamination from similar mass-to-charge ratios. The $^{13}C^{6+}$ ion beam was extracted from the ECR ion source at 17.75 kV and momentum analyzed by a 90° dipole magnet. The ion source and analyzing magnet beam line are situated on a variable potential platform which can be operated in acceleration (positive potential) or deceleration (negative potential) mode to achieve the desired final ion beam energies. For this work, the final ion beam energies ranged from 1 – 30 keV/amu (400 – 2300 km/s).

Approximately 10 – 30 nA of C^{6+} ions were incident on a gas cell interaction volume (20 cm long) as shown in Fig. 1. The H_2 target gas was introduced into the gas cell volume via a leak valve with the total pressure being monitored via

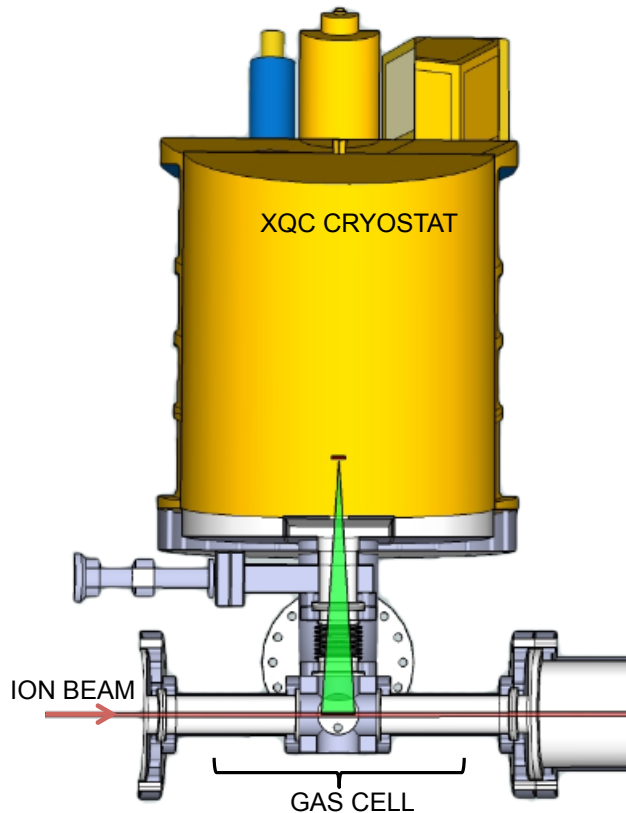


FIG. 1: (color online) Schematic of the charge exchange cell with XQC. The viewable portion of the gas cell is shown by the viewing angle from the detector array.

a nude Bayard-Alpert ion gauge and a quadrupole residual gas analyzer (SRS RGA100). The background pressure in the cell was $\simeq 10^{-8}$ Pa ($\simeq 10^{-10}$ Torr). The gas cell was held at a total pressure of $\simeq 10^{-6}$ Pa ($\simeq 10^{-8}$ Torr) during data acquisition. Due to the thermal recovery time of the detector between events, the pressure in the gas cell was adjusted slightly to restrict the x-ray count rate of the detector to < 1 Hz for given ion beam currents.

The X-ray Quantum Calorimeter (XQC) detector has been described in detail elsewhere [23, 24] so only a brief overview will be given here. The XQC is a 6×6 array of microcalorimeters with HgTe absorbers each $2.0\text{mm} \times 2.0\text{mm} \times 0.7\mu\text{m}$. This array is situated in conjunction to an adiabatic demagnetization refrigerator resulting in a final operating temperature of 50 mK. The XQC was mounted to the interaction gas cell at 90° with respect to ion beam propagation, at a distance of 23 cm from beam line center. Because of the finite size of the detector array and the physical mounting limitations, only a limited portion (2 cm) of the gas cell was viewable by the detector. This is shown schematically by the viewing cone in Fig. 1. The ions passed through this limited viewing distance in 10 – 50 ns, for the given range of velocities investigated. This allowed for detection of prompt x-rays only due to charge exchange.

Figure 2 shows a typical x-ray spectrum recorded by the XQC for C^{6+} on H_2 at a collision velocity of 400 km/s. Similar spectra were recorded over the range of collision velocities and each of the observed Lyman emission lines was peak fitted to obtain the integrated intensity of each emission line. A background spectrum, with no target gas in the gas cell, was taken at each energy to verify that there was no observable charge exchange contribution from the base residual gas of the gas cell. As can be seen in Fig. 2, the full width half maximum (FWHM) line resolution of the XQC is approximately 10 eV. Because of various filters built into the XQC, the fitted line intensities must be corrected to account for energy-dependent transmission. This was done before final Lyman line ratios were determined. The net detection efficiencies for L_α , L_β and L_γ lines are 0.065, 0.124 and 0.153, respectively.

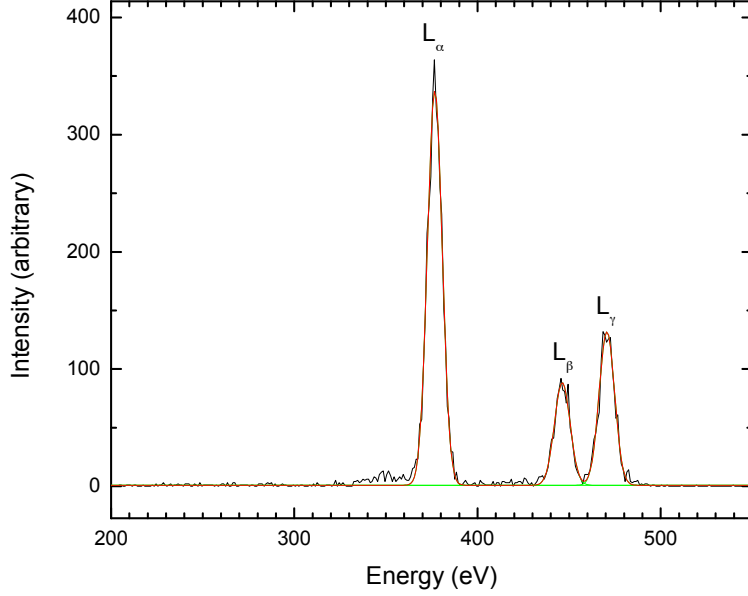


FIG. 2: (color online) Representative Lyman series line spectrum and peak fit results from charge exchange of C^{6+} and H_2 at 400 km/s. The emission line intensities have not been corrected for filter transmission.

III. RESULTS AND DISCUSSION

From Fig. 2, and the emission spectra recorded at other interaction velocities, we observed that only the L_α , L_β and L_γ emission lines contributed due to charge exchange. There was no observation of Lyman- δ or higher lines, which suggests that only principle quantum states up to $n = 4$ significantly contributed, in agreement with the CBM and the experimental VUV results of Dijkkamp et al. [17]. The results of Hoekstra et al. [18] suggest a small ($\approx 3\%$) contribution from capture to $n = 5$.

Figure 3 shows the line emission ratios of L_β/L_α and L_γ/L_α as a function of collision velocity determined from the measured x-ray spectra. Both the L_β/L_α and L_γ/L_α line ratios shown in Fig. 3 exhibit fairly constant values below 800 km/s and decrease with increasing collision velocity. At the highest measured velocity the line ratios seem to be approaching a lower constant value.

If we consider only populating $n = 2, 3$ or 4 in CX, and the resulting radiative cascades, the relative probabilities of producing L_α , L_β and L_γ line emission due to CX to C^{6+} can be determined by

$$P(L_\alpha) = \frac{\sigma_2}{\Sigma\sigma_i} s_{2,1} + \frac{\sigma_3}{\Sigma\sigma_i} (s_{3,0} + s_{3,2}) + \frac{\sigma_4}{\Sigma\sigma_i} \left(s_{4,0} \frac{A_{4,0 \rightarrow 2,1}}{\Sigma A_{4,0}} + s_{4,1} \frac{A_{4,1 \rightarrow 3,0} + A_{4,1 \rightarrow 3,2}}{\Sigma A_{4,1}} + s_{4,2} \frac{A_{4,2 \rightarrow 2,1}}{\Sigma A_{4,2}} + s_{4,3} \right) \quad (4)$$

$$P(L_\beta) = \frac{\sigma_3}{\Sigma\sigma_i} s_{3,1} \frac{A_{3,1 \rightarrow 1,0}}{\Sigma A_{3,1}} + \frac{\sigma_4}{\Sigma\sigma_i} \left(s_{4,0} \frac{A_{4,0 \rightarrow 3,1}}{\Sigma A_{4,0}} \frac{A_{3,1 \rightarrow 1,0}}{\Sigma A_{3,1}} + s_{4,2} \frac{A_{4,2 \rightarrow 3,1}}{\Sigma A_{4,2}} \frac{A_{3,1 \rightarrow 1,0}}{\Sigma A_{3,1}} \right) \quad (5)$$

$$P(L_\gamma) = \frac{\sigma_4}{\Sigma\sigma_i} s_{4,1} \frac{A_{4,1 \rightarrow 1,0}}{\Sigma A_{4,1}} \quad (6)$$

where $\frac{\sigma_n}{\Sigma\sigma_i}$ is the relative cross section for an electron being captured to principle quantum state n . The relative weighting factor of each n, l state is given by $s_{n,l}$ (the relative l -distribution normalized for each n), radiative transition A-values from state n, l to n', l' are given as $A_{n,l \rightarrow n',l'}$ (these values are given in Table I) and the total decay rate via all paths from a given n, l state is given by $\Sigma A_{n,l}$.

From these calculated emission probabilities, the line ratios L_β/L_α and L_γ/L_α can then be determined for specific $s_{n,l}$ weighting factors and relative cross sections for CX resulting in an electron in $n = 2, 3$ or 4 . These can then

TABLE I: A-values for the radiative transitions from n, l to n', l' . Data statistically averaged over j states were obtained from <http://open.adas.ac.uk>.

(n, l)	(n', l')	$A_{n,l \rightarrow n',l'} [\text{s}^{-1}]$
(2,1)	(1,0)	8.12×10^{11}
(3,0)	(2,1)	8.19×10^9
(3,1)	(1,0)	2.17×10^{11}
(3,1)	(2,0)	2.91×10^{10}
(3,2)	(2,1)	8.38×10^{10}
(4,0)	(2,1)	3.34×10^9
(4,0)	(3,1)	2.38×10^9
(4,1)	(1,0)	8.84×10^{10}
(4,1)	(2,0)	1.25×10^{10}
(4,1)	(3,0)	3.98×10^9
(4,1)	(3,2)	4.51×10^8
(4,2)	(2,1)	2.67×10^{10}
(4,2)	(3,1)	9.12×10^9
(4,3)	(3,2)	1.79×10^{10}

be compared to the line ratios shown in Fig. 3 to gauge the l -distribution model that best describes the Lyman line emission at different collision velocities.

Based on the CBM predictions, the majority of SEC is to $n = 4$. In their VUV emission measurements of CX between C^{6+} and H_2 , Dijkkamp et al. [17] showed that approximately 90% of the total capture cross section was to $n = 4$ with an upper limit of approximately 10% for capture to $n = 3$. Hoekstra et al. [18] suggested that 67% of SEC capture is to $n = 4$ and 6% to $n = 3$ with 3% to $n = 5$ and over 20% to DCAI.

In order to gauge the possible contribution of DCAI at the lower collision velocities, we look to the total CX cross sections between C^{6+} on H_2 and H measured by Meyer et al. [14]. As can be seen in Fig. 4, the absolute CX cross sections from H_2 and H are essentially the same above 500 km/s, considering the uncertainty. However, slower collision velocities show a significant decrease in the CX cross section from H while the cross section from H_2 remains relatively unchanged. Given that these measurements could not distinguish SEC and DCAI, it is likely that DCAI is a significant contributor to the cross section difference observed at the slower velocities. This suggests that in the velocity regime shown in Fig. 3, the contribution from DCAI should be no more than 20% of the total capture cross section (the uncertainty level of the total cross section measurements) at the lowest velocities and should diminish quickly at higher velocities. Mack et al. [19, 20] have shown that the principal double capture states are of the form $3lnl'$ and $4lnl'$ with $3lnl'$ being significantly more dominant which results in an electron in a $2l$ state. In terms of the Lyman emission measurements presented here, this would lead to a relative increase of L_α for those DCAI events resulting in population of the $2p$ state.

The upper pane of Fig. 5 illustrates the relative $n = 4$ weighting factors, $s_{4,l}$, for the different l -distribution models discussed in the Introduction. In Table II, we show the line ratios determined by substituting these l -distribution models into Eqns. 4–6 and considering only SEC to $n = 4$. As can be seen, none of these calculated line ratios agree with those shown in Fig. 3 over the range of velocities measured. For the velocities below 800 km/s in Fig. 3, the calculated line ratios resulting from the statistical l -distribution model seem to agree best with the measured ratios, however, even the line ratios resulting from the statistical model are considerably different than the measured line ratios. This suggests that sole SEC to $n = 4$ is not an adequate description of the overall CX.

In evaluating the l -distribution model most applicable at the low collision velocities, we consider the VUV measurements of Dijkkamp et al. [17]. The middle and lower panes of Fig. 5 show the relative weighting factors of the different l -states in $n = 4$ for N^{6+} on H_2 and O^{6+} on H_2 , respectively, at various collision energies. In comparing these l -distributions with the model distributions in the upper pane of Fig. 5, it can be seen that there seems to be a slight peak in the distributions for N^{6+} and O^{6+} around $l = 0$ and 1 for the lowest collision energies, however, O^{6+} shows a more peaked distribution for low l -states than N^{6+} , perhaps suggesting a trend towards a more statistical l -distribution for C^{6+} at these lower energies. The l distributions for N^{6+} and O^{6+} seem more even in general and clearly transition to statistical by 4–5 keV/amu. In the 4–5 keV/amu range, our line ratios begin to decrease from nearly constant values, suggesting a transition from a constant l -distribution. The line ratio plateaus we observe at low collision velocity and their disparity with the different l -distribution models, as shown in Table II, suggests that we do not observe the amount of CX to $3p$ and $4p$ states predicted by l -distributions peaked at low l -states, such

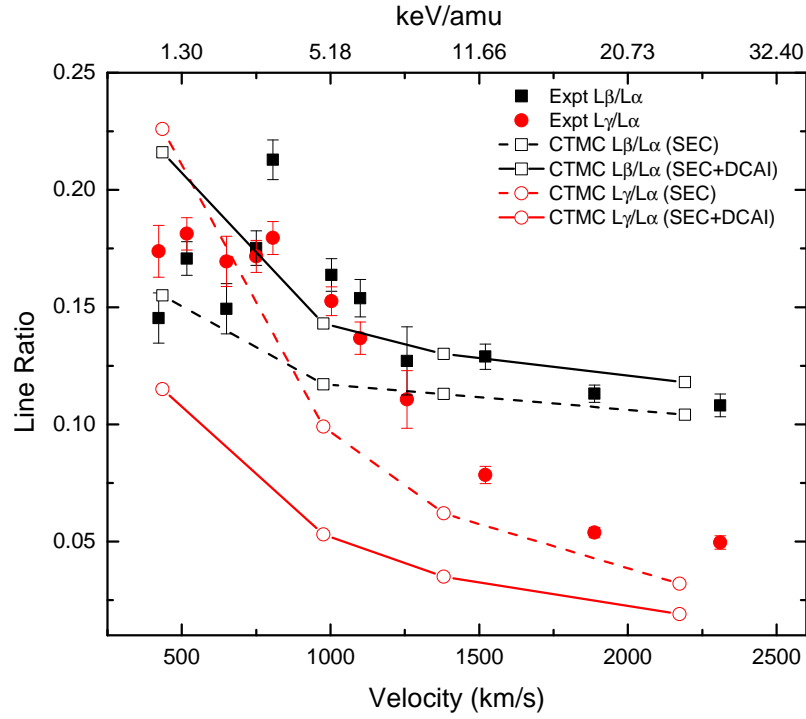


FIG. 3: (color online) Measured $L\beta/L\alpha$ (filled squares) and $L\gamma/L\alpha$ (filled circles) line ratios as a function of collision velocity. Error bars represent 2σ uncertainty. The open symbols represent CTMC calculations for SEC only (dashed joining lines) and SEC + DCAI (solid joining lines)

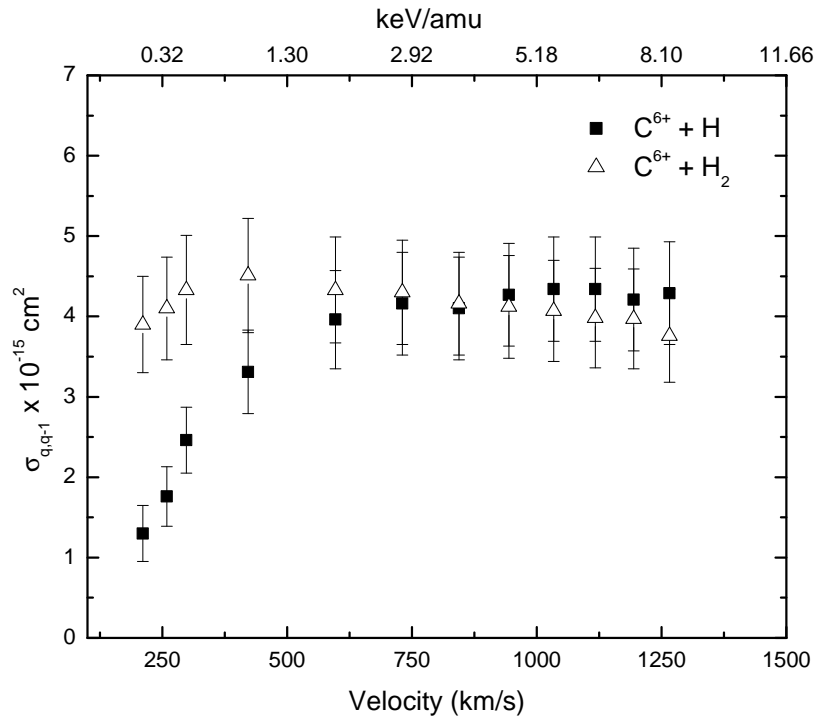


FIG. 4: Experimental total charge exchange cross sections for C^{6+} on H and H_2 measured by Meyer et al. [14].

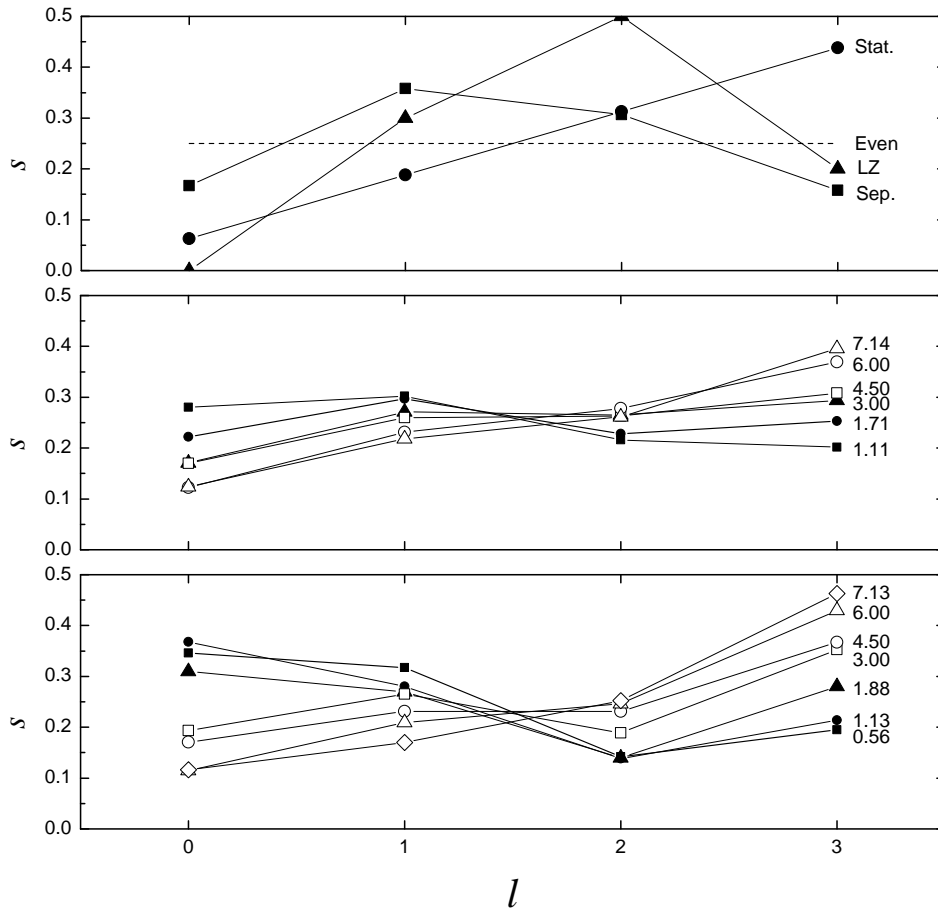


FIG. 5: The upper pane shows the different l -distribution models for $n = 4$. The middle pane shows the relative weighting factors derived from the state-selective CX cross sections of Dijkkamp et al. [17] for N^{6+} on H_2 at various energies (keV/amu). The bottom pane shows the relative weighting factors derived from the state-selective CX cross sections of Dijkkamp et al. for O^{6+} on H_2 at various energies (keV/amu).

TABLE II: Calculated Lyman line ratios resulting from SEC to $n=4$ using different l -distribution models are shown on the first four rows. The last two rows show the calculated Lyman line ratios using the normalized $n=4$ l -distributions from Fritsch & Lin [25] for $\text{C}^{6+} + \text{H}$ at 1 keV/amu and 25 keV/amu.

l -distribution Model	L_β/L_α	L_γ/L_α
Even	0.249	0.355
Statistical	0.130	0.221
Landau-Zener	0.192	0.431
Separable	0.261	0.603
$\text{C}^{6+} + \text{H}$ (1 keV/amu)	0.202	0.350
$\text{C}^{6+} + \text{H}$ (25 keV/amu)	0.070	0.101

as in the LZ and Separable l -distribution models. This suggests that the statistical l -distribution model is likely the most appropriate in this collision velocity regime. It should also be noted that the collision velocity in this range corresponds with approximately half the orbital velocity of the captured electron, which is typically considered to result in a statistical l -distribution[13].

We can now consider the relative cross sections to $n = 3$ and 4 via SEC and a possible contribution to $n = 2$ via DCAI at low collision velocities using the statistical l -distribution model. Figure 6 illustrates two forms of partitioning

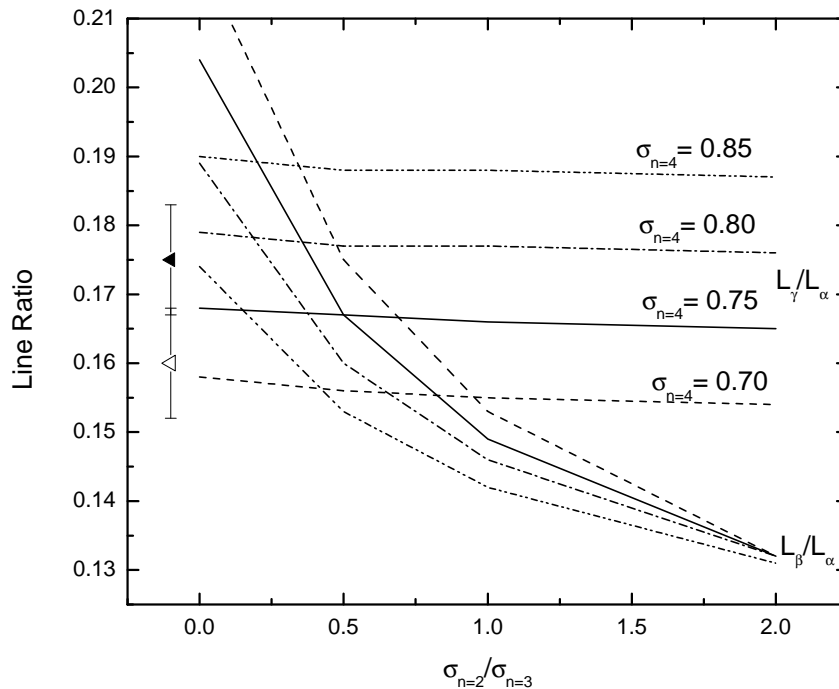


FIG. 6: Effect of relative cross section partitioning to line ratios. The line types are paired based on the relative $n = 4$ cross sections. The filled symbol on the left represents the mean L_γ/L_α ratio below 800 km/s. The open symbol represents the mean L_β/L_α line ratio below 800 km/s.

simultaneously. Each pair of linetypes represents the calculated (from Eqns. 4–6) L_β/L_α and L_γ/L_α line ratios for a fixed relative cross section for population of $n = 4$ (primary SEC capture state) from 0.70 – 0.85, which matches the range of uncertainties determined from the measured absolute cross sections in Fig. 4. The remaining relative cross section contribution is then distributed to $n = 2$ (DCAI) and 3 (SEC). The abscissa of Fig. 6 indicates how this remaining portion of the relative cross section is partitioned between $n = 2$ and 3. It can be seen from Fig. 6 that the L_γ/L_α ratio is essentially insensitive to the $n = 2$ and 3 partitioning and is only affected by the relative $n = 4$ cross section, which is reasonable given that only the $4p$ state contributes to the L_γ emission. The L_β/L_α ratio, however, is sensitive to the $n = 2$ and 3 partitioning.

In the low-velocity region of Fig. 3 where we observe the line ratios to plateau, we can now estimate the relative contributions of $n = 2, 3$ and 4. From Fig. 6 we can see that the L_γ/L_α ratio in the low-velocity region of Fig. 3 is best described by a relative cross section to $n = 4$ of approximately 0.80, resulting in a relative cross section of 0.20 distributed among $n = 2$ and 3. With the relative $n = 4$ partitioning now set, we can use the L_β/L_α ratio in the same low-velocity region of Fig. 3 to determine the $n = 2$ and 3 partitioning. This is best described by $\sigma_{n=2}/\sigma_{n=3} = 0.5$. This ultimately results in relative principal quantum state cross sections of 0.07 for $n = 2$, 0.13 for $n = 3$ and 0.80 for $n = 4$. We should point out that the 13% relative cross section for $n = 3$ is consistent with the estimated upper limit of SEC to $n = 3$ of approximately 10% reported by Dijkkamp et al. and that the 7% relative cross section to $n = 2$ seems to be a reasonable estimate of DCAI as bounded by the total cross section measurements of Meyer et al.

In the higher-velocity region of Fig. 3, above 800 km/s, the line ratios fall off with increasing collision velocity with the L_β/L_α ratio becoming larger than the L_γ/L_α ratio. This suggests that capture to $4p$ is considerably reduced at higher velocities which is indicative of capture to higher l -states in the $n = 4$ manifold. Given that the low-velocity regime is best described by a statistical l -distribution, this capture to higher l -states suggests a transition to an over-statistical distribution which peaks near the maximum l . If we use Eqns. 4–6 and assume that DCAI is negligible at the higher collision velocities while the relative $n = 3$ to $n = 4$ cross sections are constant, then the L_γ/L_α ratio at 2300 km/s is best described by a $4p$ weighting factor, $s_{n,l}$, of 0.05 while the $4d$ and $4f$ weighting factors are approximately 0.45 and 0.50, respectively. The L_β/L_α ratio near 2300 km/s is best described by a weighting factor of 0.10 for $3p$ and 0.90 for $3d$.

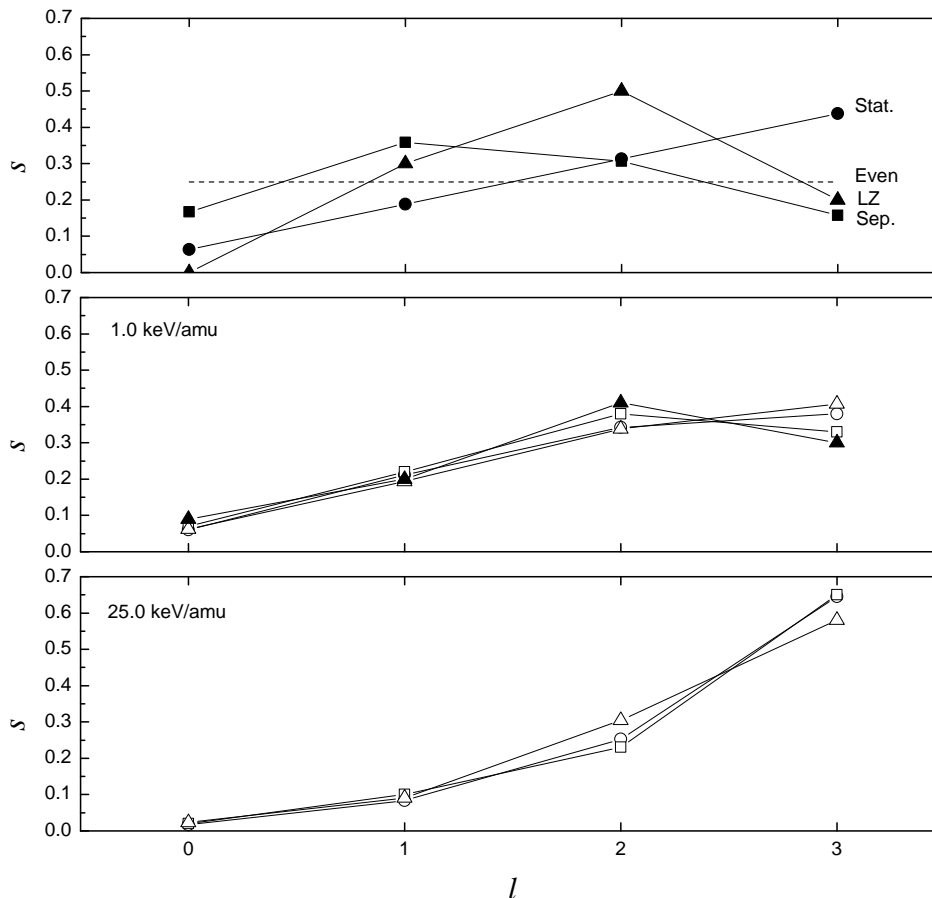


FIG. 7: The upper pane is the same as from Fig. 5 reproduced here for comparison. The middle and bottom panes show the relative weighting factors for $n = 4$ derived from the state-selective CX cross sections of Toshima & Tawara [28] (open circles), Fritsch & Lin [25] (open squares), Green et al. [29] (open triangles) and Kimura & Lin [30] (filled triangles) for C^{6+} on H at 1 keV/amu and 25 keV/amu, respectively.

Figure 3 shows the results of CTMC calculations for both the L_{β}/L_{α} and L_{γ}/L_{α} line ratios [26, 27]. As pointed out previously, the CTMC method is expected to be most applicable at the higher collision velocities. The calculations are done for the cases of SEC only and for SEC in combination with DCAI and TI, although the TI cross section contribution is an order of magnitude less than the DCAI contribution and is considered negligible. As can be seen in Fig. 3 at the higher collision velocities, the CTMC results are in relatively good agreement with the line ratios determined from the experiment and tend to be independent of the DCAI contribution, which is reasonable given that DCAI is expected to fall off quickly with increasing collision velocity. At the low collision velocities, the CTMC results considering only SEC seem to agree best with the L_{β}/L_{α} line ratio. For the L_{γ}/L_{α} ratio, the plateau observed in the experimental line ratios lies in between the CTMC results considering only SEC and SEC with DCAI.

A further comparison can be made to the resulting l -distributions for capture to $n = 4$ in CX between C^{6+} and H at different energies, although it is expected that the relative n -state populations will be slightly different given the ionization potential difference between H_2 and H. At 1 keV/amu, approximately 90% of the total capture cross section is to $n = 4$ while at 25 keV/amu, capture to $n = 5$ becomes a substantial part of the total cross section. Figure 7 shows the relative l -distributions for the $n = 4$ manifold from the data of Toshima & Tawara [28], Fritsch & Lin [25], Green et al. [29] and Kimura & Lin [30] at 1 keV/amu and 25 keV/amu collision energies. This range is comparable with our measured lower and upper energy range. As can be seen in Fig. 7, the H data at 1 keV/amu suggests that the statistical and LZ l -distributions are most predominant while at 25 keV/amu, the l -distribution population is peaked at the maximum l -state, suggesting a transition to an over-statistical distribution. As a comparison, Table II shows the L_{β}/L_{α} and L_{γ}/L_{α} line ratios calculated using the $n=4$ l -distribution data of Fritsch & Lin for capture

from atomic hydrogen at 1 keV/amu and 25 keV/amu. At 1 keV/amu, the calculated line ratios are similar to the those obtained from the LZ model. At 25 keV/amu, the line ratios are closer to those observed for capture from H₂ and are indicative of the trend to capture to higher angular momentum states at higher collision energy. We note that at the higher collision energy, the predominant capture to maximum angular momentum leads to increased L_α emission and thus lower overall line ratios with respect to L_α, as would be expected.

IV. CONCLUSION

State-specific n, l CX cross sections have been known to be highly dependent on collision velocity, however, it is still relatively difficult to predict emission spectra using the predominant l -distribution models put forth in the literature. From our measured high resolution x-ray emission spectra for CX between C⁶⁺ and H₂, and subsequently determined L_β/L_α and L_γ/L_α line ratios, we observe nearly constant line ratios at collision velocities between 400–800 km/s and decreasing line ratios with increasing collision velocity. As seen in the trend of previous VUV measurements, the low velocity regime seems to be attributed to a statistical l -distribution that progresses to an over-statistical l population at high collision velocities.

-
- [1] R. Hulse, D. Post, and D. Mikkelsen, *J. Phys. B* **13**, 3895 (1980).
 - [2] M. Mattioli, N. Peacock, H. Summers, B. Denne, and N. Hawkes, *Phys. Rev. A* **40**, 3886 (1989).
 - [3] R. Isler, *Plasma Phys. Control. Fusion* **36**, 171 (1994).
 - [4] C. Lisse, *Science* **274**, 205 (1996).
 - [5] T. Cravens, *Geophys. Res. Lett.* **24**, 105 (1997).
 - [6] P. Beiersdorfer, C. Lisse, R. Olson, G. Brown, and H. Chen, *Astrophys. J.* **549**, L150 (2001).
 - [7] H. Ryufuku, K. Sasaki, and T. Watanabe, *Phys. Rev. A* **21**, 745 (1980).
 - [8] J. Simcic, D. Schultz, R. Mawhorter, J. Cadez, J. Greenwood, A. Chutjian, C. Lisse, and S. Smith, *Phys. Rev. A* **81**, 062715 (2010).
 - [9] W. Fritsch and C. Lin, *J. Phys. B* **19**, 2683 (1986).
 - [10] M. Kimura and R. Olson, *J. Phys. B* **17**, L713 (1986).
 - [11] R. Smith, A. Foster, and N. Brickhouse, *Astron. Nachr.* **333**, 301 (2012).
 - [12] R. K. Janev and H. Winter, *Phys. Rep.* **117**, 265 (1985).
 - [13] J. Burgdörfer, R. Morgenstern, and A. Niehaus, *J. Phys. B: At. Mol. Opt. Phys.* **19**, L507 (1986).
 - [14] F. W. Meyer, A. Howald, C. Havener, and R. Phaneuf, *Phys. Rev. A* **32**, 3310 (1985).
 - [15] F. W. Meyer, A. Howald, C. Havener, and R. Phaneuf, *Phys. Rev. Lett.* **54**, 2663 (1985).
 - [16] J. Greenwood, I. Williams, S. Smith, and A. Chutjian, *Phys. Rev. A* **63**, 062707 (2001).
 - [17] D. Dijkkamp, Y. S. Gordeev, A. Brazuk, A. Drentje, and F. de Heer, *J. Phys. B: At. Mol. Opt. Phys.* **18**, 737 (1985).
 - [18] R. Hoekstra, D. Ciric, F. de Heer, and R. Morgenstern, *Phys. Scripta* **T28**, 81 (1989).
 - [19] E.M.Mack (1987), thesis, R. U. Utrecht.
 - [20] M. Mack, J. Nijland, P. Straten, A. Niehaus, and R. Morgenstern, *Phys. Rev. A* **39**, 3846 (1989).
 - [21] X. Defay, K. Morgan, D. McCammon, D. Wulf, V. Andrianarijaona, M. Fogle, D. Seely, I. Draganic, and C. Havener, *Phys. Rev. A* **88**, 052702 (2013).
 - [22] I. Draganic, D. Seely, and C. Havener, *Phys. Rev. A* **83**, 054701 (2011).
 - [23] D. McCammon, R. Almy, E. Apodaca, W. B. Tiest, W. Cui, S. Deiker, M. Galeazzi, M. Juda, A. Lesser, T. Mihara, et al., *Astrophys. J.* **576**, 188 (2002).
 - [24] D. McCammon, K. Barger, D. Brandl, R. Brekosky, S. Crowder, J. Gygas, R. Kelley, C. Kilbourne, M. Lindeman, F. Porter, et al., *J. Low Temp. Phys.* **151**, 715 (2008).
 - [25] W. Fritsch and C. Lin, *Phys. Rev. A* **29**, 3039 (1984).
 - [26] P. Stancil and D. Schultz (2013), private communication.
 - [27] A. Hasan, F. Eissa, R. Ali, D. Schultz, and P. Stancil, *Astrophys. J.* **560**, L201 (2001).
 - [28] N. Toshima and H. Tawara, *Tech. Rep.*, NIFS-DATA-26 (1995).
 - [29] T. Green, E. Shipsey, and J. Browne, *Phys. Rev. A* **25**, 1364 (1982).
 - [30] M. Kimura and C. Lin, *Phys. Rev. A* **32**, 1357 (1985).

Acknowledgments

This research is supported in part by the NASA Solar & Heliospheric Physics Program NNH07ZDA001N, NASA Grant No. NNX09AF09G, and by the Office of Fusion Energy Sciences and the Division of Chemical Sciences, Geosciences and Biosciences, Office of Basic Energy Sciences, US Department of Energy. We would like to thank

P. C. Stancil and D. R. Schultz for providing the CTMC calculation results. The authors would also like to extend a special thanks to S. D. Loch and C. Ballance for stimulating discussions and suggestions.